



RESEARCH ARTICLE

10.1002/2016JA022712

Key Points:

- We examine the LT dependence of Saturn's southern field-aligned currents in the dawn sector
- Only modest differences are found between the mean currents in the midnight and dawn-noon sectors
- The differences are insufficient to explain the peak in radio emissions in the dawn-noon sector

Correspondence to:

G. J. Hunt,
gjh19@le.ac.uk

Citation:

Hunt, G. J., S. W. H. Cowley, G. Provan, E. J. Bunce, I. I. Alexeev, E. S. Belenkaya, V. V. Kalegaev, M. K. Dougherty, and A. J. Coates (2016), Field-aligned currents in Saturn's magnetosphere: Local time dependence of southern summer currents in the dawn sector between midnight and noon, *J. Geophys. Res. Space Physics*, 121, 7785–7804, doi:10.1002/2016JA022712.

Received 17 MAR 2016

Accepted 30 JUL 2016

Accepted article online 6 AUG 2016

Published online 25 AUG 2016

Field-aligned currents in Saturn's magnetosphere: Local time dependence of southern summer currents in the dawn sector between midnight and noon

G. J. Hunt¹, S. W. H. Cowley¹, G. Provan¹, E. J. Bunce¹, I. I. Alexeev², E. S. Belenkaya², V. V. Kalegaev², M. K. Dougherty³, and A. J. Coates⁴

¹Department of Physics and Astronomy, University of Leicester, Leicester, UK, ²Skobel'syn Institute of Nuclear Physics, Lomonosov Moscow State University, Moscow, Russia, ³Blackett Laboratory, Imperial College London, London, UK, ⁴Mullard Space Science Laboratory, University College London, Dorking, UK

Abstract We examine and compare the magnetic field perturbations associated with field-aligned ionosphere-magnetosphere coupling currents at Saturn, observed by the Cassini spacecraft during two sequences of highly inclined orbits in 2006/2007 and 2008 under late southern summer conditions. These sequences explore the southern currents in the dawn-noon and midnight sectors, respectively, thus allowing investigation of possible origins of the local time (LT) asymmetry in auroral Saturn kilometric radiation (SKR) emissions, which peak in power at ~8 h LT in the dawn-noon sector. We first show that the dawn-noon field data generally have the same four-sheet current structure as found previously in the midnight data and that both are similarly modulated by “planetary period oscillation” (PPO) currents. We then separate the averaged PPO-independent (e.g., subcorotation) and PPO-related currents for both LT sectors by using the current system symmetry properties. Surprisingly, we find that the PPO-independent currents are essentially identical within uncertainties in the dawn-dusk and midnight sectors, thus providing no explanation for the LT dependence of the SKR emissions. The main PPO-related currents are, however, found to be slightly stronger and narrower in latitudinal width at dawn-noon than at midnight, leading to estimated precipitating electron powers, and hence emissions, that are on average a factor of ~1.3 larger at dawn-noon than at midnight, inadequate to account for the observed LT asymmetry in SKR power by a factor of ~2.7. Some other factors must also be involved, such as a LT asymmetry in the hot magnetospheric auroral source electron population.

1. Introduction

Electric currents flowing along magnetic field lines are of central importance in planetary magnetospheres in transferring momentum and energy between the upper atmosphere and ionosphere of the planet and the magnetospheric plasma and solar wind at large distances. With regard to Saturn's magnetosphere, the topic of the present paper, three such field-aligned current systems have been discussed theoretically to date. The first is the current system associated with subcorotation of the magnetospheric plasma, consisting of distributed downward currents over the polar region of strongly subcorotating flow, surrounded by a ring of upward current as the plasma returns to near-rigid corotation at lower latitudes mapping to the inner region of the magnetosphere [Cowley *et al.*, 2004b, 2008]. The second system is associated with the solar wind interaction, in which currents flow into the ionosphere at dusk, across the polar ionosphere and out at dawn, closing in the magnetopause boundary layers, similar to the “region 1” and “region 2” currents at Earth [e.g., Cowley, 2000] but opposite in polarity due to the opposite sense of the planetary field. Such currents, flowing near the boundary of open and closed field lines, would thus add dawn-dusk asymmetry to the overall subcorotation system [Cowley *et al.*, 2004a; Jackman and Cowley, 2006]. The third is the current system associated with the “planetary period oscillation” (PPO) phenomenon at Saturn, in which the principal currents also flow into the ionosphere on one side of the pole and out on the other, closing in the magnetosphere and opposite ionosphere, but which now rotate about the planet's spin/magnetic axis with a period close to the planet's ~10.5 h rotation period [Southwood and Kivelson, 2007; Andrews *et al.*, 2010; Southwood and Cowley, 2014]. While the underlying physical origin has yet to be elucidated, the PPO currents appear to be driven by twin-vortical flows that rotate with slightly different and slowly seasonally varying periods in the northern

©2016. The Authors.

This is an open access article under the terms of the Creative Commons Attribution License, which permits use, distribution and reproduction in any medium, provided the original work is properly cited.

and southern polar ionospheres [Jia *et al.*, 2012; Jia and Kivelson, 2012; Hunt *et al.*, 2014]. They also appear to be related to the subcorotation current system; in that, the principal PPO currents are near co-located with the upward current of the subcorotation system, and are of comparable strength, such that they essentially double the net upward current where the PPO current flows upward out of the ionosphere and reduces it near to zero where they flow down [Hunt *et al.*, 2014, 2015].

Noting the near axisymmetry of Saturn's internal planetary magnetic field [Burton *et al.*, 2010], field-aligned currents are most readily detected in the spatially structured azimuthal magnetic fields that they generate above the ionosphere [Bunce *et al.*, 2008, 2010; Talboys *et al.*, 2009a, 2009b, 2011; Southwood and Kivelson, 2009]. Ideally, these are observed on polar spacecraft orbits at small radial distances that pass rapidly between the "polar void" region of open field lines at highest latitudes [e.g., Gurnett *et al.*, 2010; Jinks *et al.*, 2014] and lower latitudes mapping to the inner part of magnetosphere, thus providing a near-"snapshot" latitude profile of the field perturbations produced by the currents at the local time (LT) of the pass. As the radial distance of the orbit increases, however, the magnitude of the field perturbations falls, the duration of the passes increases, and the spacecraft may not cross the field lines associated with the inner part of the current system. In the case of Saturn, the radial distance of such a pass should not exceed $\sim 10 R_s$ if the main part of the current system is to be observed, at which distance field lines in the equatorial magnetosphere map to $\sim 17.5^\circ$ colatitude from the northern pole in the northern ionosphere and to $\sim 19.5^\circ$ colatitude from the southern pole in the southern ionosphere [Hunt *et al.*, 2014, 2015]. (R_s is Saturn's 1 bar equatorial radius equal to 60,268 km.)

During the Cassini mission to date, there have been three such near-optimum orbital intervals which allow Saturn's field-aligned currents to be studied, two of which occurred during southern summer conditions in 2006/2007 and 2008, prior to vernal equinox in August 2009, while the third occurred during northern spring in 2012/2013. The first of these explored the dawn to noon sector in the southern hemisphere and the dusk to midnight sector in the northern hemisphere, while the second and third principally explored northern and southern currents in the midnight sector. The latter two data sets will thus allow, in future work, exploration of seasonal effects in the midnight sector in both hemispheres. Here, however, we use the first two of these data sets to examine LT variations in the southern summer hemisphere spanning midnight (2008 data) to dawn-noon (2006/2007 data), a topic of particular interest since this range includes the sector of peak Saturn kilometric radio (SKR) emissions centered near 8 h LT [Lamy *et al.*, 2009], as will be discussed further below.

In Figure 1 we thus show 4 years of spacecraft orbit and other relevant data spanning calendar years 2006–2009 inclusive. Year boundaries are marked at the top of the figure, while time in days is shown at the bottom, where $t=0$ corresponds to 00:00 UT on 1 January 2004. The red vertical dashed line shows the time of Saturn vernal equinox in August 2009. The black and white bars at the top of the figure show the duration of each spacecraft orbital revolution (Rev), defined from apoapsis to apoapsis and numbered every 10 Revs at the time of periapsis. In Figure 1a the vertical lines show the latitudinal range of each Rev plotted at the time of periapsis, together with the latitude of periapsis shown by the black circle. As indicated above, two intervals of highly inclined orbits are evident, the first spanning late 2006 to early 2007 and the second spanning 2008 and the first half of 2009. In Figure 1b the vertical lines similarly show the radial range of each spacecraft Rev on a log scale, also plotted at the time of periapsis. During the first interval of highly inclined orbits in 2006/2007, the radial distance of periapsis was sufficiently small to allow observations of much of the field-aligned current structures at both the beginning and end of the interval (radial distances less than $\sim 10 R_s$) but was raised during the central part of the interval such that at most only the outer (high-latitude) part of the currents could be observed. Suitable Revs to observe the currents during this first interval are thus confined to Revs 30–36 in late 2006 and Revs 41–44 in early 2007, shown by the vertical dashed lines and the gray shaded areas in the figure. These are the intervals studied previously by Talboys *et al.* [2009a] and in part by Southwood and Kivelson [2009]. We note that Bunce *et al.* [2008] also studied current signatures from Rev 37 in early 2007, for which concurrent Hubble Space Telescope ultraviolet (UV) auroral images were also available. However, as noted by these authors, periapsis on this Rev was at a sufficiently large radial distance ($\sim 13 R_s$) that only the outer part of the current region was crossed. During the second sequence of high-latitude orbits, however, the radius of periapsis was initially sufficiently low that the full auroral current system was crossed on a sequence of more than 30 orbits, corresponding to Revs 59–95 as also marked by the dashed vertical lines and the gray shaded area in Figure 1, spanning most of

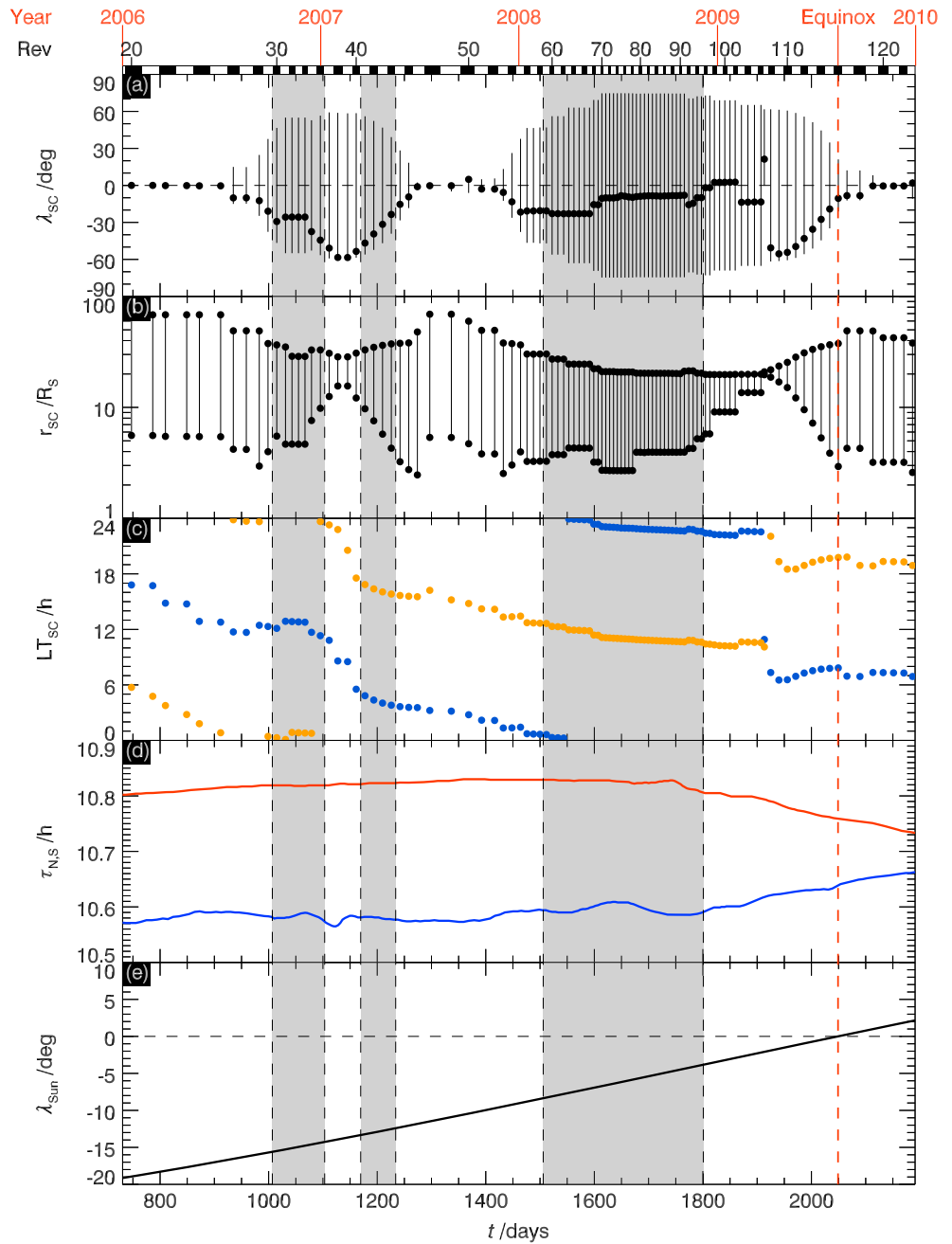


Figure 1. (a–e) Overview of Cassini orbital parameters for the interval spanning 2006 to 2009 inclusive, together with PPO-related and seasonal parameters. Time in days is given at the bottom of the plot, where $t = 0$ corresponds to 00 UT on 1 January 2004, while year boundaries are indicated in red at the top. The time of vernal equinox (11 August 2009) is also shown at the top of the figure and marked by the vertical red dashed line in the plot. The black and white bars at the top of the plot indicate the duration of each Cassini Rev, defined from apoapsis to apoapsis, and numbered every 10 Revs at the time of periapsis. The vertical bars in Figure 1a show the latitude range of the spacecraft on each Rev (deg), plotted at the time of periapsis, together with the latitude of periapsis indicated by the black circle. The vertical bars in Figure 1b similarly show the radial distance range on each Rev (R_s), plotted by using a log scale. Figure 1c shows the LT (hours) of periapsis (blue) and apoapsis (orange) on each Rev. Figure 1d shows the periods (hours) of the southern (red) and northern (blue) PPO oscillations determined by *Andrews et al.* [2012]. Figure 1e shows the latitude of the Sun at Saturn (deg), passing through zero at vernal equinox. The gray shaded regions highlight the intervals of highly inclined Cassini orbits whose data are employed in this study.

2008. These data were discussed both individually and statistically by *Talboys et al.* [2009b, 2011] and *Bunce et al.* [2010] and more recently by *Hunt et al.* [2014, 2015]. Later in the second high-latitude interval, extending into 2009, the periapsis distance was again beyond $\sim 10 R_S$, such that traversals of the auroral field lines were slower and partial [*Bunce et al.*, 2014], and thus less suitable for the present study.

In Figure 1c we plot the LT of apoapsis (orange) and periapsis (blue) for each Rev, the latter indicating to a first approximation the LT of the near-periapsis crossing of auroral field lines in the two hemispheres. During the first interval of high-latitude passes in 2006/2007, the LT of periapsis was initially located near noon and later predawn, which combined with the inclination of the orbit provided near-periapsis coverage of southern auroral field lines between predawn and postnoon, ~ 3 to ~ 13 h LT, as indicated above. During the second high-latitude interval, periapsis was located near midnight, providing southern auroral region crossings between ~ 23 and ~ 4 h LT, modestly overlapping the 2006/2007 data in the predawn sector. Overall, the southern data thus span the dawn sector between pre-midnight and postnoon. The previous studies cited above have demonstrated that the field perturbations observed throughout this LT sector show consistent signatures of plasma subcorotation at high southern latitudes nearest the pole, with “lagging” azimuthal fields associated with distributed downward currents, which relax to small values at lower latitudes associated with a ring of upward current co-located with the auroral region [*Bunce et al.*, 2008; *Talboys et al.*, 2011; *Hunt et al.*, 2014]. A lagging field implies that field lines are bent out of meridian planes toward earlier LTs at larger distances, with negative azimuthal fields in the northern hemisphere and positive azimuthal fields in the southern hemisphere, associated with the transfer of angular momentum from the atmosphere to the magnetosphere. Superposed modulations of comparable amplitude associated with the PPOs are also observed throughout this sector [*Talboys et al.*, 2009a; *Southwood and Kivelson*, 2009; *Hunt et al.*, 2014]. Here, however, we make a first quantitative comparison of the subcorotation and PPO-related field perturbations observed in the midnight and dawn-noon sectors.

Additional relevant information is shown in Figures 1d and 1e. Figure 1d shows the southern (red) and northern (blue) PPO periods over the 4 year interval, obtained from analysis of magnetic field data by *Andrews et al.* [2012]. It can be seen that the periods are near-constant and well separated over the two Cassini high-latitude intervals, with southern and northern periods of ~ 10.8 and ~ 10.6 h, respectively. Convergence toward a near-common period over the equinox interval began near the end of the second interval studied here. *Hunt et al.* [2014, 2015] demonstrated that modulation of the southern currents was dominated by the southern PPO system during the 2008 interval, with little evidence of dual modulation at the northern period, unlike corresponding conditions in the northern hemisphere. Since it was found by *Andrews et al.* [2012] that the northern system was weaker relative to the southern in equatorial data surrounding the 2006/2007 high-latitude interval than during the 2008 interval (north/south amplitude ratios of ~ 0.4 in 2006/2007 compared with ~ 0.9 in 2008), we may anticipate that the southern currents during the 2006/2007 interval were also dominantly modulated by the southern PPO system, and not by the northern system, as will be confirmed in section 2 below.

In Figure 1e we also show the latitude of the Sun at Saturn, indicating the seasonal conditions prevailing during the two high-latitude intervals, which correspond to late southern summer in both cases. The solar latitude changed from -16° to -13° across the first interval, and from -8° to -4° across the second, and reached zero, corresponding to vernal equinox, on 11 August 2009. Similar solar illumination conditions of the southern upper atmosphere thus prevailed during the two intervals, with a central region of the polar cap being permanently illuminated, extending to $\sim 14^\circ$ colatitude during the first interval and to $\sim 6^\circ$ during the second, while the southern auroral region centered near $\sim 18^\circ$ underwent day-night cycles, being sunlit between ~ 03 h and ~ 21 h LT via noon during the 2006/2007 interval, and between ~ 05 and ~ 19 h LT during the 2008 interval, and in darkness in the remaining region via midnight. Similarity in both PPO and seasonal conditions thus renders plausible the search for LT effects in the subcorotation and PPO-related currents in the southern data set for the two intervals combined, spanning midnight to noon via dawn.

The physical significance of this range of LT is indicated in Figure 2, where we plot the variation of averaged SKR power versus LT, normalized to peak values near ~ 08 h LT, taken from *Lamy et al.* [2009]. SKR is primarily extraordinary mode emission, beamed in a thin hollow cone at a large angle to the field lines, generated by the cyclotron maser instability of accelerated auroral electrons in regions of upward directed field-aligned current [*Lamy et al.*, 2010, 2011; *Mutel et al.*, 2010]. SKR source regions, intense upward field-aligned currents,

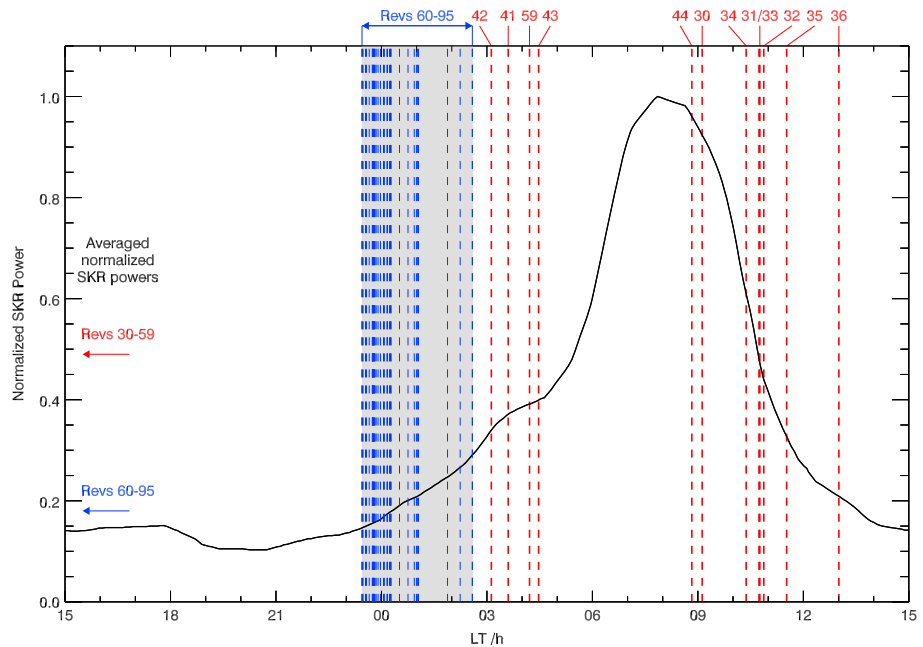


Figure 2. Plot showing the variation of averaged SKR power versus LT (h), normalized to peak values near ~08 h LT, taken from *Lamy et al.* [2009]. The superposed vertical dashed lines show the LT of the center of the main upward current sheet observed on each Cassini pass through the southern auroral region, labeled by the Rev numbers at the top of the figure. Revs 30–44 correspond to the 2006/2007 interval of high-latitude orbits and 59–95 to the 2008 interval. The 2008 data from Revs 60–95 are combined together to form the midnight data set spanning ~23–03 h LT (blue dashed lines and gray-shaded band), while the 2006/2007 data are combined with Rev 59 from 2008 to form the dawn-noon data set spanning ~03–13 h LT (red dashed lines). Exceptions are Revs 30 and 44 for which we show the LT of the equatorward boundary of the main upward current sheet (boundary 3; see Figure 5) since the poleward boundary and hence center were not clearly discerned, and Rev 41 which explored only the poleward part of the current region, for which we show the LT of the poleward boundary (boundary 1; see Figure 5b). Averaged normalized powers for the two data sets are shown by the arrows on the left of the plot as indicated, red for the dawn-noon data (Revs 30–59), and blue for the midnight data (Revs 60–95).

and UV emissions are thus expected to be co-located on the same auroral field lines. In order to derive the SKR LT power profile in Figure 2, remotely sensed direction-resolved SKR intensities obtained between mid-2004 and mid-2008 from a wide range of Cassini observation points have been mapped from their inferred source regions (where the wave and electron gyrofrequencies are equal), along magnetic field lines down into the auroral ionosphere, and have been averaged in 5° bins of longitude in the co-latitude range between 10° and 20° where most of the sources lie (see *Lamy et al.* [2009] for full details). *Southwood and Kivelson* [2009] have proposed that the strongly peaked dominant sources in the mid-morning sector result from the LT dependence of the region 1 currents associated with the solar wind interaction, directed upward in this sector and hence potentially associated with enhanced precipitation of accelerated auroral electrons and consequent emissions, and that the dominant SKR modulations arise as the upward and downward currents of the rotating PPO system become periodically superposed.

The vertical dashed lines in Figure 2 indicate the LTs of the southern hemisphere auroral region crossings during the two high-latitude intervals discussed above, as indicated by the Rev numbers at the top of the figure, Revs 30–44 for 2006/2007, and Revs 59–95 for 2008. Specifically, we show the LTs of the centers of the main upward field-aligned current regions observed on each Rev, noting from the above discussion that the upward current regions should be co-located with the sources generating the SKR emission. Exceptions are Revs 30 and 44 where only the equatorward part of the current region was clearly crossed such that we mark the LT of the equatorward boundary of the main upward current sheet (boundary 3; see section 2.3) and Rev 41 where only the poleward part of the current region was crossed such that we mark the LT of its poleward boundary (boundary 1; see section 2.3). The gray shaded region spanning LTs from ~23 to ~3 h LT contains most of the Revs during the 2008 interval, specifically Revs 60–95, which form our “midnight” data set (blue dashed lines). The remaining Revs, consisting of the 2006/2007 data plus Rev 59 from 2008, then span

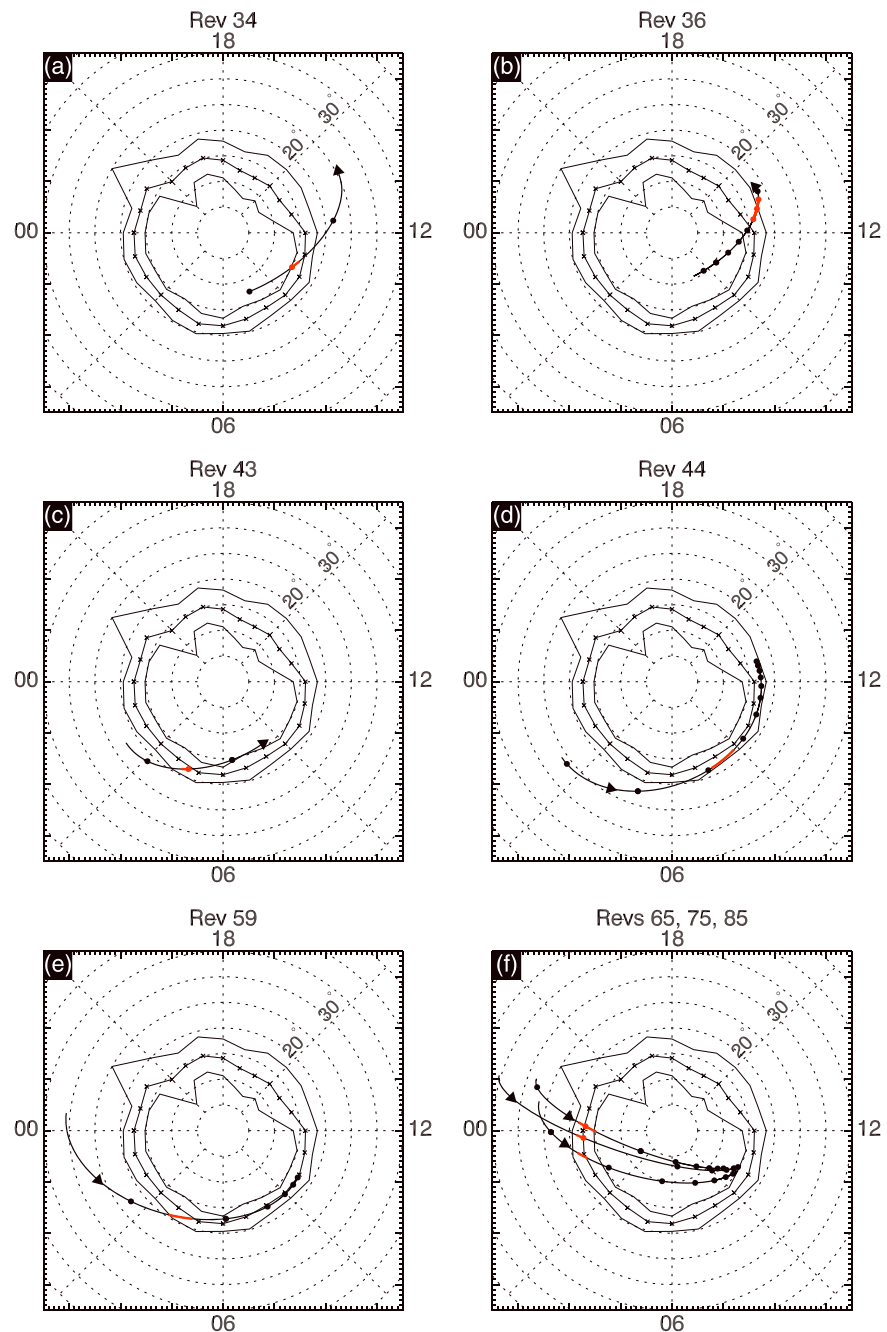


Figure 3. Southern hemisphere trajectories of the Cassini spacecraft from representative Revs shown mapped along model field lines into the southern ionosphere. The trajectories are shown on a grid of 5° colatitude measured from the southern spin/magnetic axis and 3 h of LT, viewed through the planet from the north with noon to the right and dawn at the bottom. The field model employed consists of the internal field model of *Burton et al.* [2010], together with the ring current model of *Bunce et al.* [2007] corresponding to a radial distance of the subsolar magnetopause of 22 R_S . The ionosphere is taken to be located 1000 km above the 1 bar planetary reference spheroid. The trajectories are superposed on the mean southern UV auroral region derived by *Carbary* [2012] from Cassini UVIS data, where the center line (with crosses) shows the peak intensity and the outer lines the half power points. (a–d) Trajectories from the 2006/2007 interval of highly inclined Revs, specifically for Revs 34, 36, 43, and 44, respectively, noting that the trajectories for Revs 31–33 are closely similar to that for 34. (e) The trajectory for Rev 59 from the 2008 interval of high latitude passes; (f) three representative cases from the remaining 2008 data set spanning Revs 60–95, specifically for Revs 65, 75, and 85. The arrow on each trajectory indicates the direction of travel, the black circles show markers at 2 h intervals, and the red section of the trajectory corresponds to the main upward current region (sheet 2).

LTs from ~03 to ~13 h LT and form our “dawn-noon” data set (red dashed lines). The emitted SKR powers corresponding to these Revs are generally significantly larger than those corresponding to the midnight sector. Averaging the normalized SKR powers at the LTs indicated for Revs 60–95 yields a value of $\langle p \rangle \approx 0.18$, while similarly, averaging the powers for Revs 30–36, 41–44, and 59 yields $\langle p \rangle \approx 0.49$ (using the LTs of either the centers or boundaries of the main upward current sheet as available), a factor of ~2.7 times higher. These mean values are indicated on the left of the figure. Here we examine whether differences in either the PPO-independent (subcorotation) or PPO-related currents between these LT sectors can account for these variations in emitted power.

In the following section we briefly overview the data set and analysis procedures and provide an initial comparison of the field-aligned currents observed in the midnight and dawn-noon data. In section 3 we derive the averaged subcorotation and PPO current profiles for these sectors, while in section 4 we examine whether the observed differences can account for the LT variations in SKR power shown in Figure 2.

2. Data Set and Analysis Procedures

2.1. Data Set

Our primary data set consists of 1 min averaged measurements (mean values) of the azimuthal magnetic field on southern auroral field lines for Revs 30–36 and 41–44 during the 2006/2007 Cassini high-latitude interval, previously discussed by *Talboys et al.* [2009a], together with corresponding data for Revs 59–95 during the 2008 high-latitude interval, previously discussed by *Talboys et al.* [2009b, 2011] and *Hunt et al.* [2014]. Of the latter data, two Revs are missing due to data gaps (Revs 70 and 71), while four others have been excluded (as in *Hunt et al.* [2014]) as showing atypical signatures which do not follow the general trends (Revs 66, 77, 89, and 94). As also indicated in section 1, we further combine the data for Rev 59 with the 2006/2007 data set due to its near-dawn crossing of the auroral field lines (Figure 2) to form the dawn-noon data set of 12 southern auroral passes (Revs 30–36, 41–44, and 59), while the remaining 30 southern passes of the 2008 data set form the midnight data set (Revs 60–95, excluding those mentioned above). In Figure 3 we show representative trajectories mapped along field lines into the southern ionosphere, shown on a grid of 5° colatitude measured from the southern spin/magnetic axis and 3 h in LT, viewed “through” the planet from the north with noon to the right and dawn at the bottom. The field model employed to map the trajectories consists of the three-term axisymmetric internal field model of *Burton et al.* [2010], together with the axisymmetric ring current model of *Bunce et al.* [2007], the latter corresponding to an intermediate subsolar magnetopause distance of 22 R_s . The “ionosphere” is taken to be located 1000 km above the 1 bar planetary reference spheroid. The mapped trajectories are shown superposed on the mean southern ultraviolet (UV) auroral region derived by *Carbary* [2012] from an analysis of Cassini Ultraviolet Imaging Spectrograph (UVIS) data, where the crosses and straight lines show the position of peak emission and the outer lines the half-power points (see figure caption for details). Specifically, Figures 3a and 3b show the mapped trajectories for Revs 34 and 36 that crossed the southern auroral oval close to noon (Revs 31–33 are near-identical to Rev 34), Figures 3c and 3d show the trajectories for Revs 43 and 44 that crossed the oval predawn and postdawn (only partially in the latter case), while Figure 3e shows the trajectory of Rev 59, the first Rev of the 2008 data set, that also crossed the oval predawn. Figure 3f then shows representative trajectories from the later 2008 data set, specifically Revs 65, 75, and 85, that crossed the oval in the midnight sector. The black circles are shown along the trajectories at 2 h intervals so that the rapidity of the crossings can be gauged, while the arrows indicate the direction of travel. The red segments on each trajectory indicate the position of the main sheet of upward directed field-aligned current observed on each pass (see section 2.3), which can be seen generally to correspond to the UV auroral oval.

In Figure 4 we also show color-coded trajectories mapped into meridian planes by using cylindrical (ρ , z) coordinates, where z is the distance along the planet’s spin/magnetic axis and ρ is the perpendicular distance from the axis. Figure 4a shows the trajectories of the dawn-noon data set, while Figure 4b shows representative examples from the midnight data set (as in Figure 3f). The black arrowed lines on which these are superimposed are those of the field model employed in the Figure 3, shown at 5° intervals of southern ionospheric colatitude between 0° and 30°, while the red and blue regions show the locations of the four main sheets of southern field-aligned current (unmodulated by the PPO system) found by *Hunt et al.* [2014] from an analysis of the 2008 southern data. The blue areas marked 1 and 3 show the two regions of downward field-aligned

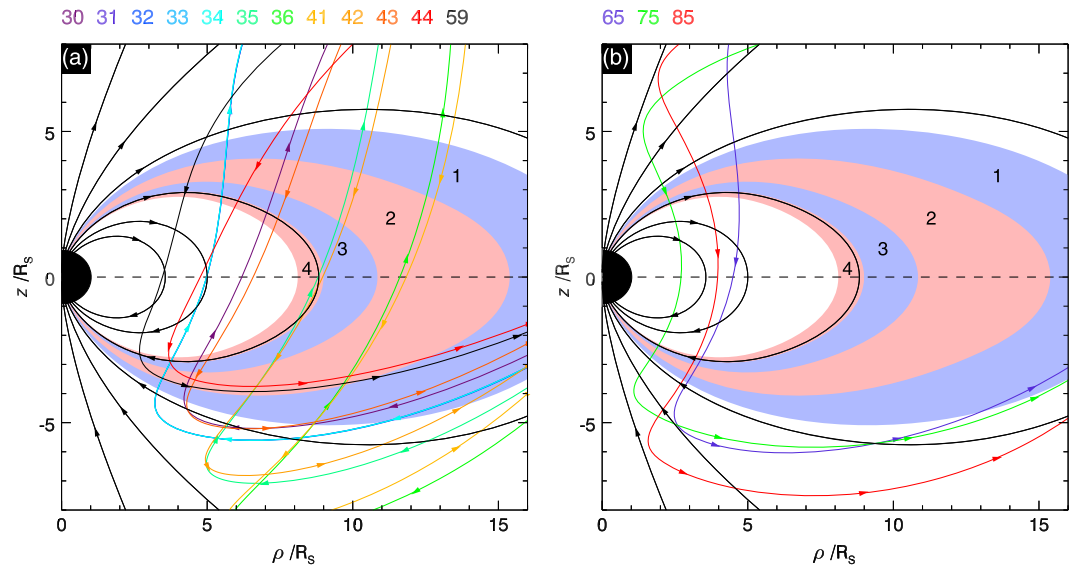


Figure 4. Cassini trajectories projected onto a magnetic meridian plane using cylindrical (ρ, z) coordinates, where z is distance along the planet’s spin/magnetic axis positive northward and ρ is the perpendicular distance from the axis. (a) The trajectories of the 2006/2007 Revs employed in this study, Revs 30–36 and 41–44, plus Rev 59 from 2008, forming the dawn-noon data set. (b) Three representative trajectories from the remainder of the 2008 Revs, specifically for Revs 65, 75, and 85 (as in Figure 3f). The trajectories are color-coded as indicated at the top of each figure, and the arrows indicate the direction of travel. The black arrowed lines show model field lines starting at 5° intervals of southern colatitude between 0° and 30° . The colored bands, also bounded by field lines, show the averaged locations of the four PPO-independent field-aligned current sheets determined from 2008 southern hemisphere data by *Hunt et al.* [2014], numbered from pole to equator as shown, where the red and blue colors represent the currents directed upward and downward relative to the southern ionosphere. The main auroral upward current corresponds to sheet 2. Their attenuated extension into the northern ionosphere, as shown, was demonstrated by *Hunt et al.* [2015].

current with respect to the southern ionosphere, while the red areas marked 2 and 4 show the two regions of upward current, with region 2 being the main upward current associated with the auroral oval. Though these current sheets were derived from the near-midnight 2008 data, as we will show, they also provide a useful initial guide at the other LTs examined here. It can be seen from Figure 4a that a majority of the Revs in the dawn-noon data set provide a clear crossing of the (averaged 2008) current layers in the southern hemisphere, particularly of main upward current sheet 2. Some, however, only provide partial coverage, but can still give useful information on the location and azimuthal field at some of the current sheet boundaries, which can be used in subsequent analysis. Examples include Rev 36, which crossed only the outer current sheets in the southern hemisphere, and Rev 44, which crossed only the inner sheets (see also Figure 3). It can also be seen in Figure 4b that the representative Revs in the midnight data set all provide clear near-planet traversals of southern auroral field lines.

2.2. Data Analysis Procedures

The data analysis procedures follow those previously given in detail by *Hunt et al.* [2014, 2015], such that only a brief outline will be given here. Starting from the 1 min averaged values of the azimuthal magnetic field, B_ϕ , the initial step is to estimate and subtract the contribution to this field from non-field-aligned current sources, principally those associated with the magnetopause and tail currents, given the near-axisymmetry of the planetary and inner ring current fields [*Burton et al.*, 2010; *Kellett et al.*, 2011]. For this purpose we have employed azimuthal field values computed along the spacecraft trajectory by using the “intermediate” Saturn magnetospheric model derived by *Belenkaya et al.* [2008], which, as for the field model employed in Figures 3 and 4, assumes a subsolar magnetopause distance of $22 R_s$. These values are first subtracted from the observed data, such that all future reference to field data and products derived therefrom refers to this “corrected” data. It should be noted, however, that as for the 2008 data studied by *Hunt et al.* [2014, 2015], the observed azimuthal field perturbations associated with the auroral field-aligned currents are on the order of ~ 10 nT in the 2006/2007 data set, while the subtracted model field values are ~ 1 nT or less, such that the “correction” is generally small and does not affect the character of the data.

The second step is to map the corrected azimuthal field along auroral field lines into the ionosphere, thereby normalizing the data obtained at differing radial distances from the planet (Figure 4), and allowing an immediate estimate to be made of the associated ionospheric meridional current. To do this we take $\rho B_\phi \approx$ constant along auroral field lines between the field-perpendicular closure currents in the southern ionosphere on one side and the near-equatorial magnetosphere (or northern ionosphere) on the other, where ρ is again the perpendicular distance from the spin/magnetic axis. This approximation is exact in the case of an axisymmetric current system like that expected for plasma subcorotation but should also be approximately valid in cases where the longitudinal scale is much greater than the latitudinal scale, i.e., for sheet-like currents as anticipated here (see Appendix B of *Hunt et al.* [2014]). The azimuthal field just above the ionosphere is then given by

$$B_{\phi i} = B_\phi \left(\frac{\rho}{\rho_i} \right), \quad (1)$$

where B_ϕ is the corrected measured value at perpendicular distance ρ and ρ_i is the perpendicular distance at the foot of the field line in the ionosphere. The primary parameter employed here, however, is the meridional horizontal ionospheric current per radian of azimuth flowing at the feet of the field lines, taken positive directed from the southern pole toward the equator, given by

$$I_m = \frac{\rho_i B_{\phi i}}{\mu_0} \approx \frac{\rho B_\phi}{\mu_0}, \quad (2)$$

where μ_0 is the permeability of free space. This current, principally a Pedersen current, is that which switches off the field perturbation below the southern ionosphere. Again, assuming that azimuthal variations can be neglected compared with latitudinal variations, current continuity shows that the total field-aligned current per radian of azimuth flowing between colatitudes θ_1 and θ_2 with respect to the southern pole is given (for $\theta_2 > \theta_1$) by

$$I_{\parallel} \approx I_m(\theta_2) - I_m(\theta_1), \quad (3)$$

where the sign of I_{\parallel} gives the direction of the current with respect to the background field. If I_m increases with southern colatitude such that $I_m(\theta_2) > I_m(\theta_1)$, then I_{\parallel} is positive indicating a downward current into the southern ionosphere, while if I_m decreases with the southern colatitude, such that $I_m(\theta_2) < I_m(\theta_1)$, then I_{\parallel} is negative indicating an upward current out the southern ionosphere.

2.3. Representative Examples

In Figure 5 we show data from two representative southern passes during the 2006/2007 high-latitude interval, plotted versus colatitude θ_S measured from the southern pole over the range from 12° to 26° spanning both sets of observations, chosen particularly to illustrate different conditions of southern PPO phase. Figure 5a shows data from Rev 34, which crossed auroral field lines in the prenoon sector (Figure 3a), while Figure 5b similarly shows data for Rev 43, which crossed auroral field lines in the predawn sector (Figure 3c). The panels of each figure show, from top to bottom, (i) a Cassini Plasma Spectrometer-Electron Spectrometer (CAPS-ELS) electron count rate spectrogram covering the energy range of ~ 0.6 eV–28 keV, color coded as shown in the upper right of the figure; (ii) the ionospheric meridional current per radian of azimuth I_m (MA rad^{-1}) obtained from equation (2); and (iii) the southern PPO phase Ψ_S (deg). The southern PPO phase is given by

$$\Psi_S(\varphi, t) = \Phi_S(t) - \varphi, \quad (4)$$

where $\Phi_S(t)$ is the azimuth of the rotating equatorial quasi-uniform PPO perturbation field associated with the southern system at any time, derived from magnetic field observations by *Andrews et al.* [2012], and φ is the azimuth of the observer (i.e., the Cassini spacecraft). Both azimuths are measured from noon increasing in the sense of planetary rotation. The PPO-related azimuthal field perturbations then vary as $\sim \sin \Psi_S$ at any point in the equatorial magnetosphere and as $\sim -\sin \Psi_S$ at any point in the polar magnetosphere, such that given the geometry of the currents which cause these perturbations as outlined in section 1, the main PPO-related current should be directed downward into the southern ionosphere at $\Psi_S \sim 90^\circ$ and upward out of the ionosphere at $\Psi_S \sim 270^\circ$, as found by *Hunt et al.* [2014].

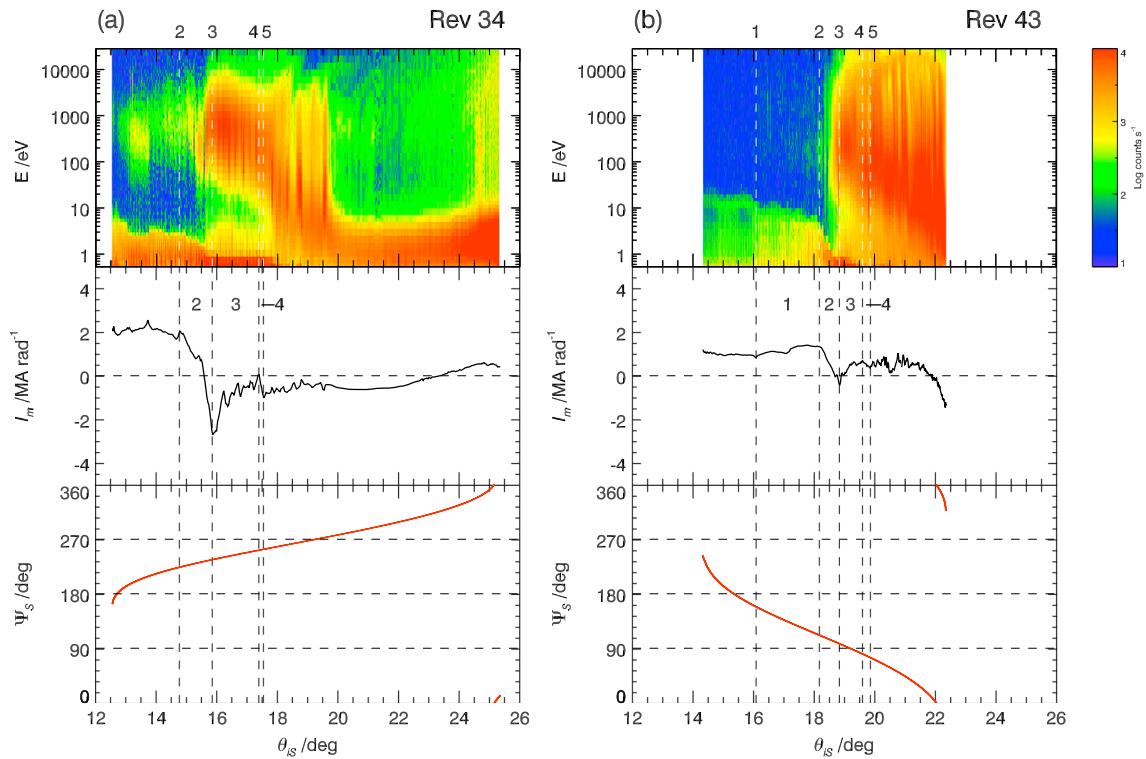


Figure 5. (a and b) Representative southern colatitude profiles from the dawn-noon data set, specifically for Rev 34 in Figure 5a exemplifying conditions for southern PPO phase $\Psi_S \sim 270^\circ$ and for Rev 43 in Figure 5b exemplifying conditions for $\Psi_S \sim 90^\circ$. The panels of each figure show, from top to bottom, (i) a CAPS-ELS electron count rate spectrogram from central anode 5 covering the energy range of ~ 0.6 eV–28 keV, color coded as shown in the upper right of the figure; (ii) the ionospheric meridional current per radian of azimuth I_m (MA rad^{-1}) calculated from the corrected observed azimuthal magnetic field using equation (2); and (iii) the southern PPO phase Ψ_S (deg) obtained from *Andrews et al.* [2012] and equation (4). These are plotted versus ionospheric colatitude from the southern pole, θ_{IS} (deg), over the range 12° – 26° spanning the data. The vertical dashed lines mark the boundaries of four sheets of field-aligned current, numbered from pole to equator as shown at the top of the figures, with the sheets themselves being similarly numbered from pole to equator as shown in the center panel of each figure. Regions in which I_m increases with θ_{IS} correspond to downward currents (sheets 1 and 3), while regions in which I_m decreases with θ_{IS} correspond to upward currents (sheets 2 and 4). In the case of Figure 5a the trajectory did not extend sufficiently far poleward to allow boundary 1 to be observed.

The vertical dashed lines in Figures 5a and 5b delineate the intervals of (in general) four main auroral region current sheets, identified by extrema in the I_m values, labeled as boundaries 1–5 from pole to equator at the top of the figures. The current sheets themselves are also labeled 1–4 from pole to equator, as shown in the middle panel of each figure, such that sheet 1 lies between boundaries 1 and 2, and so on. As for the midnight data studied by *Hunt et al.* [2014], sheets 1 and 3 correspond to downward currents where I_m increases with increasing southern colatitude (equation (3)) and sheets 2 and 4 to upward currents where I_m decreases with increasing colatitude, with sheet 2 being the main upward current. These currents are identifiable in both profiles shown, with the exception of sheet 1 for Rev 34, for which the trajectory did not extend sufficiently far poleward for the poleward boundary of sheet 1 to be clearly identified. Otherwise, these examples illustrate our overall finding that the southern currents in the dawn-noon data set generally display a similar four-sheet structure as found previously in the midnight data set by *Hunt et al.* [2014].

Examining these profiles in more detail, it can be seen that in both cases the I_m values are consistently positive at the smallest southern colatitudes observed, indicative of lagging fields and plasma subcorotation in the polar region, and fall eventually to smaller values at larger southern colatitudes, indicative of the presence of a net upward current across the auroral current region, as described for the subcorotation system in section 1. The upward current flows on closed field lines mapping to the outer region of hot magnetospheric electrons, as seen in the electron spectrograms. However, the positive polar values are larger for Rev 34 than for Rev 43, while the values at larger colatitudes in the region beyond the current sheets are negative for Rev 34 and positive for Rev 43, such that the net upward current is much larger in the former case than in the latter, $\sim 2.5 \text{ MA rad}^{-1}$ for Rev 34 and $\sim 0.5 \text{ MA rad}^{-1}$ for Rev 43. This relates to the differing southern PPO

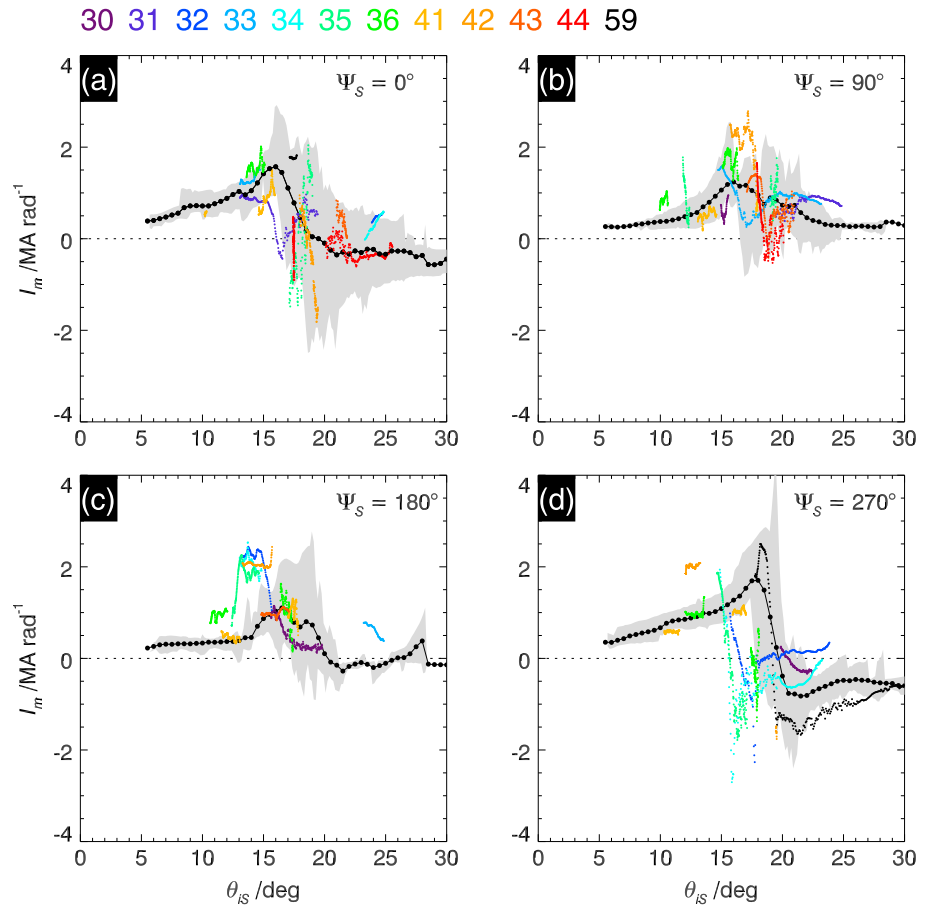


Figure 6. Overview comparison of ionospheric meridional current profiles, I_m (MA rad^{-1}) plotted versus southern ionospheric colatitude θ_{IS} (deg), for the dawn-noon and midnight data sets. The data are divided into four nonoverlapping 90° ranges of southern PPO phase Ψ_S , centered at (a) 0° , (b) 90° , (c) 180° , and (d) 270° , respectively, as shown in the top right corner of each panel. The black circles joined by the black lines show profiles for the midnight data set, averaged (mean values) in 1° bins of colatitude at steps of 0.5° , while the surrounding gray-shaded area shows the envelope formed by the overall midnight data set. The profiles of the dawn-noon data are overplotted, color-coded as shown at the top of the figure, where the purple, blue, and green colors correspond to near-noon data and the orange, red, and black colors (for Rev 59) to dawn data.

phases prevailing during these passes, with an additional net upward PPO-related current being superposed for Rev 34 under $\Psi_S \sim 270^\circ$ conditions and an additional net downward PPO-related current being superposed for Rev 43 under $\Psi_S \sim 90^\circ$ conditions, as discussed above. However, as found previously by *Hunt et al.* [2014], the field variations in both cases are clearly not monotonic across the overall current region, indicative of the presence of more structured currents than this discussion might imply. In particular, in the case of Rev 34 I_m initially falls to strongly negative values across main upward current sheet 2, corresponding to “leading” fields associated with plasma supercorotation, before returning rapidly across downward current sheet 3 toward smaller negative and near-zero values at larger colatitudes. In the case of Rev 43, I_m reduces to only small negative values across upward current sheet 2 before increasing again to small positive values across downward current sheet 3. In section 3 we elucidate the implications of these profiles for the structure of both the PPO-independent (subcorotation) and PPO-related current profiles in the dawn-noon sector. However, these examples also clearly illustrate our general finding that the dawn-noon currents exhibit similar PPO-related modulations as found in the midnight data set by *Hunt et al.* [2014].

2.4. Overview Comparison of Dawn-Noon and Midnight Data

In Figure 6 we provide an overview comparison of the colatitude current profiles for the dawn-noon data with the profiles for the midnight data previously studied by *Hunt et al.* [2014]. In the latter paper the data were

divided into eight nonoverlapping 45° ranges of southern PPO phase Ψ_S . Here, however, due to the fewer number of dawn-noon passes, we employ four nonoverlapping 90° Ψ_S ranges, centered on 0°, 90°, 180°, and 270°, shown in Figures 6a–6d. The black dots joined by black lines in each figure show the mean I_m profiles for the midnight data for these Ψ_S ranges, specifically averages (mean values) in overlapping 1° colatitude bins evaluated every 0.5°. Figures 6a and 6c show the approximately PPO-independent current profiles for the ranges centered on $\Psi_S = 0^\circ$ and 180° , respectively, in which I_m increases gradually with colatitude in the polar region associated with a distributed downward current, then more rapidly across downward current sheet 1 centered at $\sim 15^\circ$ colatitude, before falling to smaller values across main upward sheet 2 centered at $\sim 18^\circ$, corresponding to expectations for the subcorotation system discussed in section 1 (secondary downward and upward sheets 3 and 4 are largely smoothed away in these profiles). Figure 6b for Ψ_S centered on 90° then shows a smoothed double-peaked profile with little net current flow across the auroral current sheet region, similar to Rev 43 in Figure 5b, while Figure 6d for Ψ_S centered on 270° shows a large transition from positive to negative values across this region indicative of a large net upward current flow, similar to Rev 34 in Figure 5a. The gray areas surrounding these averaged profiles then show the envelopes formed by the whole of the midnight data set, indicating the generally significant level of fluctuations in the current profiles from pass to pass, particularly in the central current sheet region.

The data from the dawn-noon passes are then shown overplotted on the midnight profiles in Figure 6, colored-coded as shown at the top of the figure, where we note that the purple, blue, and green colors correspond to the near-noon passes and oranges and reds to near-dawn, while Rev 59, also near dawn, is shown in black. Here we have not included data from intervals where the spacecraft footprint moved with near-constant colatitude such that Ψ_S changed significantly for small changes in θ_{is} , leading to significant fluctuations in the I_m profiles, particularly within the auroral current region as the current sheets vary with time. Specifically, we have not included data from intervals in which Ψ_S changed by more than 90° per degree of colatitude. Overall, it can be seen that the dawn-noon data have comparable amplitudes and form to the midnight data, in so far as that can be discerned within the significant variability in the data. It is evident, for example, that the I_m values in the range centered on $\Psi_S = 90^\circ$ remain positive and elevated within the central current region, as for the midnight data, while the I_m values in the range centered on $\Psi_S = 270^\circ$ undergo a major transition from positive to negative values with increasing colatitude. It is also clear, particularly in the data in the 180° and 270° ranges, that the current profiles in the noon sector (purple, blue, and green colors) are displaced poleward of those in the midnight data by $\sim 3^\circ$ colatitude, though there is less evidence of such a displacement in the near-dawn data (oranges, reds, and black). These differences evidently relate to shifts in the effective center of the auroral oval from the planet's spin/magnetic axis toward midnight and dawn, as found in UV image data by *Nichols et al.* [2008] and *Carbary* [2012] (see, e.g., Figure 3), which needs to be taken into account in further analysis.

3. Four-Current Sheet Analysis of Dawn-Noon and Midnight Data

Due to the modest number of Revs in the dawn-noon data set compared with the midnight data set, combined with the comparable variability in the data seen in Figure 6, it is clearly inappropriate to analyze these data by taking averages. Instead, we employ an alternative approach adopted by *Hunt et al.* [2014] (their section 5), in which the main current sheet properties observed on each pass are considered individually, and averaged to determine typical current profiles within specified ranges of Ψ_S . We again note that the Ψ_S values employed here are those derived by *Andrews et al.* [2012], which we have checked against the oscillations occurring in the southern near-equatorial field data from the dawn-noon passes, specifically data mapping to southern colatitudes between 22° and 29°. Excellent agreement has been found, within $\sim 10^\circ$ of phase. In addition, no evidence was found for modulations of these data with the northern phase Ψ_N , as may be expected from the results of *Hunt et al.* [2015] for the 2008 (midnight) data set, and the relatively weaker northern oscillations that were present during the 2006/2007 interval [*Andrews et al.*, 2012].

For each spacecraft Rev contributing to the dawn-noon data we have thus determined both the meridional current value I_m and the southern colatitude θ_{is} of each of the current sheet boundaries that could reliably be identified, as illustrated in the examples in Figure 5. The I_m values are shown in the first row of Figure 7, where Figures 7a–7e show the values for each of the boundaries numbered sequentially from the pole to the equator, as in Figure 5, plotted versus the simultaneous value of Ψ_S at the boundary. Figures 7f–7j similarly show

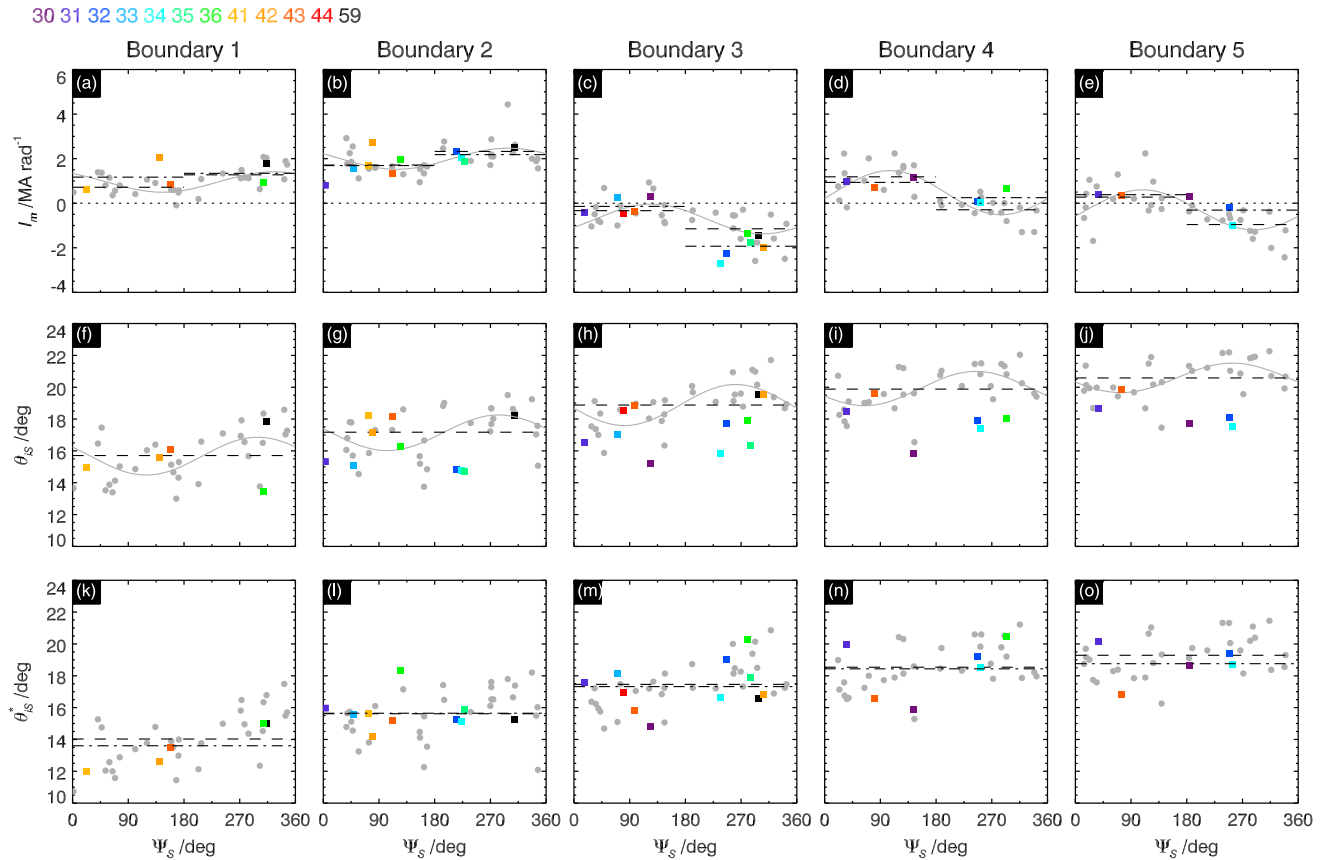


Figure 7. Plots showing the ionospheric meridional current, southern colatitude, and transformed southern colatitude at the five current sheet boundaries, as indicated along the top of the figure, plotted versus southern PPO phase Ψ_S . The squares show data from the dawn-noon data set color-coded as shown at the top of the figure, while the gray circles show the data from the midnight data set as previously studied by *Hunt et al.* [2014] (minus Rev 59). (a–e) The meridional current per radian of azimuth I_m (MA rad^{-1}) at each boundary. The gray lines show the sinusoidal fits to the midnight data from *Hunt et al.* [2014], while the dashed and dash-dotted lines show the averaged (mean) values over 180° Ψ_S ranges centered on $\Psi_S = 90^\circ$ and 270° for the midnight and dawn-noon data, respectively. (f–j) The southern ionospheric colatitude θ_S (deg) at each boundary, where the gray line again shows a sinusoidal fit to the midnight data from *Hunt et al.* [2014], and the dashed line shows the averaged value. (k–o) The southern colatitude values transformed to an axis displaced from the planet’s spin/magnetic axis by 3° colatitude toward 4 h LT, θ_S^* (deg). The dashed and dash-dotted lines show the averaged values of the midnight and dawn-noon data, respectively.

the corresponding southern colatitudes θ_S , also plotted versus Ψ_S . The colored squares in each panel show the dawn-noon data, color-coded as shown at the top of the figure (as in Figure 6), such that the purple, blue, and green colors again correspond to near-noon passes and the orange, red, and black colors to near-dawn. The gray circles in each panel then show the midnight data, to which a simple sinusoid has been least-squares fitted, as in *Hunt et al.* [2014].

Examining first the I_m values, the general variation from boundary to boundary is evident, corresponding to the nature of the field-aligned current that flows between them. For example, the current at boundary 2 is generally large and positive (equatorward), while that at boundary 3 is either near-zero or negative (poleward), this change corresponding to main upward current sheet 2 that flows between these boundaries. The PPO-related modulations of the current are also evident, varying approximately as $-\sin \Psi_S$ at boundaries 1 and 2, and as $\sin \Psi_S$ at boundaries 3 to 5, corresponding to an additional downward current being present between boundaries 2 and 3 for $\Psi_S \sim 90^\circ$ and an additional upward current for $\Psi_S \sim 270^\circ$, as discussed in section 2. It can also be seen that there is no clear distinction between the near-dawn and near-noon data, such that these will be considered together in the analysis that follows. It can further be seen that these data generally lie within the scatter of the midnight current values, such that there is no very distinctive difference between them. In the analysis reported by *Hunt et al.* [2014], the sinusoidal fits to the midnight data (plus Rev 59) were evaluated and compared in eight 45° intervals of Ψ_S . Due to the smaller number of equally

scattered dawn-noon data points here, however, we take the robust but less refined approach of averaging the midnight and dawn-noon I_m values in two 180° ranges centered on $\Psi_S = 90^\circ$ and 270° , associated with principal PPO-related currents that are directed downward and upward, respectively. These averages (mean values) are shown in Figures 7a–7e by the dash-dotted lines for the dawn-noon data and by the dashed lines for the midnight data. It can be seen that these averages are generally close together, with the exception of the $\Psi_S \sim 270^\circ$ data for boundary 3, which shows larger average negative values for the dawn-noon data than for the midnight data, corresponding to a larger upward current in sheet 2 in this case. The dawn-noon data continue generally to lie within the scatter of the midnight data in this regime, but the smaller current values observed within the midnight data are not represented in the dawn-noon data, resulting in a more negative average.

Turning now to the corresponding southern colatitude values shown in Figures 7f–7j, two effects are apparent, additional to the general equatorward displacement from boundary to boundary. The first is that the midnight data display a quasi-sinusoidal variation with Ψ_S at each boundary, as shown by the sinusoidal fits. The variation is approximately as $-\sin \Psi_S$ with an amplitude of $\sim 1^\circ$ colatitude, as reported by *Hunt et al.* [2014]. It is not obvious whether a related oscillation is also present in the dawn-noon data. However, it is seen that the near-dawn data (orange, red, and black colors) generally lie between the central and equatorward portion of the midnight data, while the near-noon data (purple, blue, and green colors) generally lie well poleward, as noted in section 2.4 in relation particularly to Figures 6c and 6d. These shifts are indicative of the current sheets, approximated as arcs of a circle, having their centers shifted toward midnight and dawn relative to the planet's spin/magnetic axis. Such shifts have previously been found in southern UV auroral data by *Nichols et al.* [2008], who reported shifts of $\sim 2^\circ$ colatitude toward 3–4 h LT. Similarly, using the UV auroral data shown here in Figure 3, *Carbary* [2012] found a shift of 3.6° toward 2.5 h LT from a circular fit to the southern data and 2.4° toward 4.3 h LT from harmonic analysis. Here we have transformed the position data to an axis displaced by 3° colatitude toward 4 h LT, yielding modified southern colatitudes denoted by θ_{IS}^* , which we find satisfactorily renders the mean of the dawn-noon and midnight data closely comparable, as shown in Figures 7k–7o, which we henceforth employ here. In these panels the means of the dawn-noon data are shown by the dash-dotted lines and the means of the midnight data by the dashed lines, which are seen to be essentially indistinguishable for central boundaries 2 to 4.

To analyze these data further, *Hunt et al.* [2014] compared current profiles with “opposite” values of Ψ_S , differing by 180° , in their case at 45° steps of Ψ_S . Assuming that the PPO-related current is equal and opposite in such cases, the PPO-independent (subcorotation) current can be determined by taking half of the sum of the two profiles, thus eliminating the PPO current, while the PPO-related current can be determined by taking the half of their difference, thus eliminating the PPO-independent current. First, however, the current sheets at differing Ψ_S were appropriately “lined up” by subtraction of the overall sinusoidal oscillation in colatitude that is evident in the midnight data in Figures 7f–7j. To a good first approximation, however, this procedure simply renders the position values for each boundary close to their mean values for all Ψ_S . Here therefore we take a simpler more direct approach by taking the mean current values at each boundary in the upper row of Figure 7 to apply to the mean transformed boundary positions in the third row of the figure.

Results are shown in Figure 8a, where we plot the mean I_m values at each boundary for the 180° Ψ_S ranges centered on 90° (blue) and 270° (red) versus the corresponding mean transformed southern colatitude θ_{IS}^* , for both the noon-dawn data (solid lines) and the midnight data (dashed lines). The error bars show the standard error of the mean values derived from the contributing data points in Figure 7. It can be seen that the average dawn-noon and midnight profiles are generally very similar within uncertainties in both Ψ_S ranges. For the $\Psi_S = 270^\circ$ profiles, however, I_m has a larger negative value at boundary 3 for the dawn-noon data, $\sim -1.9 \text{ MA rad}^{-1}$, than for the midnight data, $\sim -1.1 \text{ MA fsrad}^{-1}$, as previously noted, while having a more positive value at boundary 4, $\sim 0.25 \text{ MA rad}^{-1}$ compared with $\sim -0.30 \text{ MA rad}^{-1}$. On average, upward sheet 2 and downward sheet 3 (as marked at the top of the figure) thus carry larger field-aligned currents at dawn-noon than at midnight, but not by large factors.

As indicated above, to estimate the PPO-independent current profiles for the two LT sectors, we take half the sum of the $\Psi_S = 90^\circ$ and $\Psi_S = 270^\circ$ profiles for the two cases, with results shown in Figure 8b for the dawn-noon (solid lines) and midnight (dashed lines) data. It can be seen that the profiles are almost identical in the two cases, certainly within estimated uncertainties. The midnight profile is also very similar to those

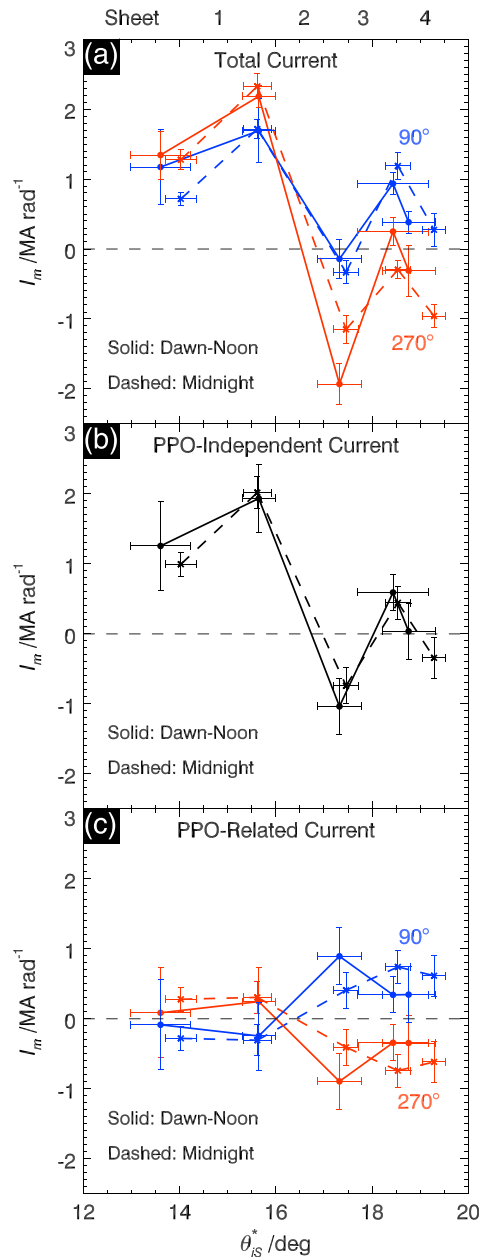


Figure 8. Overall colatitude profiles of ionospheric meridional current per radian of azimuth I_m (MA rad^{-1}), derived from the mean I_m values at each current sheet boundary shown in Figures 7a–7e and the mean transformed southern colatitudes θ_S^* (deg) shown in Figures 7k–7o. Current sheet numbers are indicated at the top of the figure. (a) Profiles for the $180^\circ \Psi_S$ ranges centered on 90° (blue) and 270° (red), where the dawn-noon profiles are shown by the circles joined by the solid lines, and the midnight profiles by crosses joined by the dashed lines. The error bars show the standard error of the mean values in Figure 7. (b) The PPO-independent I_m profiles for both the dawn-noon data (circles and solid lines) and midnight (crosses and dashed lines), derived by taking the sum of the two corresponding Ψ_S profiles in Figure 8a (separated by 180° of Ψ_S), and dividing by two. (c) The PPO-related I_m profiles in a similar format, determined by subtracting the two Ψ_S profiles in Figure 8a and dividing by two, where the blue profiles correspond to the Ψ_S range centered on 90° , and the equal and opposite red profiles to the Ψ_S range centered on 270° . The error bars in Figures 8b and 8c were determined by combining the corresponding errors in Figure 8a.

determined previously from the 2008 data by *Hunt et al.* [2014] (their Figures 14e–14h), as may be expected, once allowance is made for the colatitude transformation employed here. Surprisingly therefore these results provide no support for the suggestion by *Southwood and Kivelson* [2009] that the higher modulated SKR powers emitted in the dawn-to-noon sector (Figure 2) result from the superposition of the PPO-related upward current on a quasi-steady current system that has larger upward currents at dawn-noon than at dusk-midnight, whether those currents result from the solar wind interaction or otherwise. Instead, the results in Figure 8b indicate that the PPO-independent currents are approximately independent of LT in the midnight to noon sector via dawn, thus most likely related to general subcorotation of magnetospheric plasma apparently uninfluenced by solar wind-related effects.

Similarly, to estimate the PPO-related currents from the profiles in Figure 8a, we subtract the $\Psi_S = 90^\circ$ (blue) profile from the $\Psi_S = 270^\circ$ (red) profile (or vice versa) for each of the two LT regimes and divide the result by two. These profiles are shown in Figure 8c, where the blue profiles correspond to the $180^\circ \Psi_S$ range centered on 90° , and the equal and opposite red profiles correspond to the $180^\circ \Psi_S$ range centered on 270° . Again, the solid lines correspond to the dawn-noon profiles and the dashed lines to the midnight profiles. We thus note that addition of the solid and dashed blue ($\Psi_S = 90^\circ$) profiles in Figure 8c to the solid and dashed PPO-independent (black) profiles in Figure 8b reproduces the solid and dashed blue ($\Psi_S = 90^\circ$) profiles in Figure 8a, while addition of the solid and dashed red ($\Psi_S = 270^\circ$) profiles in Figure 8c to the solid and dashed PPO-independent (black) profiles in Figure 8b reproduces the solid and dashed red ($\Psi_S = 270^\circ$)

profiles in Figure 8a. The profiles for the midnight sector are again similar to those determined by *Hunt et al.* [2014] (see their Figure 14k), given both the colatitude transformation and the averaging over a wider range of Ψ_S values, here 180° rather than 45° in *Hunt et al.* [2014]. In this context we note that if the PPO-related perturbations do vary sinusoidally as $\pm \sin \Psi_S$, then averaging over 180° ranges centered on 90° and 270° will result in values that correspond to ~ 0.64 of the peak values, while the related factor for 45° ranges centered on 90° and 270° as employed by *Hunt et al.* [2014] is ~ 0.97 . To estimate peak values at 90° and 270° from the profiles in Figure 8c the values shown should thus be multiplied by a factor of $\sim (1/0.64) \approx 1.6$. Comparison of the dawn-noon and midnight profiles in Figure 8c then indicates slightly larger peak principal currents flowing in a narrower layer at dawn-noon compared with midnight, together with a clear current of reversed sense and smaller magnitude flowing at large colatitudes (as also found in the northern hemisphere data by *Hunt et al.* [2015]), these differences being those that give rise to the differences in the dawn-noon and midnight profiles seen in Figure 8a.

4. Implications for LT Variations in Auroral Emission Power

The results in the previous section show that the auroral currents observed in the dawn-noon and midnight sectors are similar, though with an indication of a somewhat larger upward current for $\Psi_S \sim 270^\circ$ in the dawn-noon sector compared with midnight. It is evident from Figure 2, however, that the averaged SKR emission at the LTs corresponding to the dawn-noon passes is significantly larger than that associated with the midnight passes. Specifically, we recall the discussion in section 1 which showed that the averaged normalized power corresponding to the dawn-noon passes is $\langle p \rangle \approx 0.49$, compared with $\langle p \rangle \approx 0.18$ for the midnight passes, thus corresponding to a factor of ~ 2.7 . Given that the emitted SKR power corresponds to $\sim 1\%$ of the precipitating electron power [e.g., *Lamy et al.*, 2010, 2011], this suggests that the power of the auroral electron precipitation is similarly on average a factor of ~ 2.7 larger at the locations of the dawn-noon passes than at the midnight passes. We thus consider to what extent the modest differences in the current profiles in Figure 8a might account for these differences.

To do this we apply *Knight's* [1973] theory of auroral electron acceleration by field-aligned electric fields in regions of upward directed field-aligned currents to the main upward directed current sheets in Figure 8a, noting that the current densities implied, on the order of $\sim 100 \text{ nA m}^{-2}$, considerably exceed that which can be supplied by unaccelerated hot magnetospheric electrons $\sim 10 \text{ nA m}^{-2}$ [e.g., *Bunce et al.*, 2008; *Cowley et al.*, 2008]. The precipitating energy flux of accelerated electrons is then given by the *Lundin and Sandahl* [1978] formula

$$E_f = \frac{E_{f0}}{2} \left[\left(\frac{j_{||i}}{j_{||i0}} \right)^2 + 1 \right], \quad (5)$$

where $j_{||i}$ is the field-aligned current density just above the ionosphere and $j_{||i0}$ is the maximum current density that can be carried by unaccelerated magnetospheric electrons assumed isotropic, given by

$$j_{||i0} = eN \left(\frac{W_{th}}{2\pi m_e} \right)^{\frac{1}{2}}, \quad (6)$$

where N is the number density and W_{th} the thermal energy (both constants along a field line if isotropic), e and m_e are the electron charge and mass, and E_{f0} is the unaccelerated precipitating energy flux given similarly by

$$E_{f0} = 2NW_{th} \left(\frac{W_{th}}{2\pi m_e} \right)^{\frac{1}{2}}. \quad (7)$$

The total current flowing into or out of the ionosphere per radian of azimuth in each current sheet in Figure 8a is given by the difference in I_m values at the boundaries of the sheet, ΔI_m (see equation (3)). The corresponding field-aligned current density is then

$$j_{||i} \approx \frac{\Delta I_m}{\Delta A_i} \approx \frac{\Delta I_m}{R_i^2 \sin \theta_i \Delta \theta_i}, \quad (8)$$

where ΔA_i is the corresponding ionospheric area per radian of azimuth given by $\Delta A_i \approx R_i^2 \sin \theta_i \Delta \theta_i$, where R_i is the polar radius of the ionosphere, θ_i is the southern colatitude at the center of the current sheet, and $\Delta \theta_i$ is

the current sheet co-latitudinal width. The current densities for the main upward current sheet (sheet 2) implied by the values in Figure 8a are on the order of $\sim 100 \text{ nA m}^{-2}$ as indicated above. Substituting equation (8) into equation (5), and neglecting the second term in the brackets for the case $(j_{\parallel i}/j_{\parallel i0})^2 \gg 1$, the energy flux can be written as

$$E_f \approx \frac{E_{f0}}{2} \left(\frac{\Delta I_m}{R_i^2 \sin \theta_i \Delta \theta_i j_{\parallel i0}} \right)^2, \quad (9)$$

such that the total precipitating electron power per radian of azimuth $\varepsilon_f = E_f \Delta A_i$ is given by

$$\varepsilon_f \approx \frac{E_{f0}}{2R_i^2 j_{\parallel i0}^2} \left(\frac{\Delta I_m^2}{\sin \theta_i \Delta \theta_i} \right). \quad (10)$$

If we then take for sake of argument that the magnetospheric electron parameters are the same for the mid-night and dawn-noon current layers, the variation in the precipitating electron power per radian of azimuth associated specifically with variations in the upward current region is given by

$$\varepsilon_f \approx k \frac{\Delta I_m^2}{\sin \theta_i \Delta \theta_i}, \quad (11)$$

for some constant k . We thus consider the quantity (with units $\text{MA}^2 \text{ rad}^{-2} \text{ deg}^{-1}$)

$$P = \frac{\Delta I_m^2}{\sin \theta_i \Delta \theta_i} \quad (12)$$

as a proxy giving the variation in precipitating electron power per radian of azimuth, and hence also in the auroral emission, due to variations in the properties of the upward current sheet.

Applying equation (12) to main upward current sheet 2 in Figure 8a, we find that the power proxy values (in the above units) for the midnight data are ~ 8.3 for the Ψ_5 range centered on 90° and ~ 23.4 for the Ψ_5 range centered on 270° . Similarly, the values for the dawn-noon data are ~ 7.1 for the Ψ_5 range centered on 90° and ~ 35.5 for the range centered on 270° . Comparing the powers for the two Ψ_5 ranges in these LT sectors, we first note that for the dawn-noon data the power at $\Psi_5 \sim 270^\circ$ is estimated to be a factor of ~ 5 larger than at $\Psi_5 \sim 90^\circ$, while for the midnight data this ratio falls modestly to a factor of ~ 3 . Such values are in reasonable agreement with the results of *Nichols et al.* [2010], who found that UV emissions in the morning sector are ~ 3 times more intense under the former condition than under the latter. Similar comparisons are more difficult for SKR emissions, due to the difficulty of deconvolving the variations in intrinsic SKR powers from highly variable source visibility effects.

Similarly, comparing the powers in the two LT intervals for given Ψ_5 ranges, we second note that the current profiles are consistent with near-equal auroral power outputs at dawn-noon and midnight for the range centered on $\Psi_5 \sim 90^\circ$, but with outputs which are a factor of $\sim (35.5/22.5) \approx 1.6$ larger at dawn-noon than at midnight for the range centered on $\Psi_5 = 270^\circ$. Given also that the SKR powers shown in Figure 2 correspond to averaged powers and that the two Ψ_5 ranges persist for equal intervals of time, we estimate from the currents that the average precipitation power at dawn-noon should only be factor of ~ 1.3 times larger than at midnight based on the mean current profiles alone, thus clearly insufficient to account for the estimated difference in the averaged SKR powers at these LTs of a factor of ~ 2.7 .

We thus conclude that some other factors must also be involved in producing the observed LT variation in SKR power, such as some more subtle (e.g., non linear) property of the current system or LT variations in the source electron parameters. With regard to the latter possibility, we note that the total precipitating electron power per radian of azimuth ε_f in equation (10) depends not only on the current parameters as discussed above but also on the electron source parameters, previously taken to be constant for sake of argument. Substituting from equations (6) and (7) into equation (10) and ignoring physical constants, we find

$$\varepsilon_f \propto \frac{E_{f0}}{j_{\parallel i0}^2} \propto \frac{\sqrt{W_{th}}}{N}, \quad (13)$$

such that for fixed current parameters, the precipitating energy flux increases as the auroral electron source population becomes hotter and/or more tenuous. Further investigation of this possibility awaits future work beyond the remit of the present study.

5. Summary and Conclusions

We have investigated the southern hemisphere signatures of auroral field-aligned currents observed during the 2006/2007 high-latitude interval of Cassini orbits and have compared these with the signatures observed in the 2008 high-latitude interval studied previously by *Hunt et al.* [2014]. An important difference between these data sets lies in the LT coverage of the crossings of the auroral region, in the predawn to postnoon sector for the 2006/2007 data (plus Rev 59 from 2008), but in the midnight sector for the remaining 2008 data. This difference is significant due to the strong variation in SKR power that occurs within it, peaking near ~ 8 h LT, but falling to, e.g., $\sim 30\%$ of the peak at ~ 03 h LT on one side and at ~ 12 h LT on the other [*Lamy et al.*, 2009]. Since this variation should reflect related variations in the power of the precipitating electrons responsible for the emission, a likely cause lies in a LT variation in the upward directed field-aligned currents, in which auroral electrons are accelerated into the atmosphere by field-aligned electric fields, as suggested by *Southwood and Kivelson* [2009] in relation to the effect of LT-dependent currents driven by the solar wind interaction.

We have first shown that the currents in the dawn-noon sector generally have the same four-sheet structure as those found by *Hunt et al.* [2014] in midnight data, with the principal upward current associated with auroral emissions being the most poleward upward sheet in the sequence. A distributed downward current also flows in the polar region poleward of these structured current sheets. Second, we have shown that these currents are modulated by the southern PPO system in the same way as those at midnight found by *Hunt et al.* [2014], involving the superposition of an additional downward current for phases around $\Psi_S \sim 90^\circ$ and an upward current for $\Psi_S \sim 270^\circ$, thus attenuating the main upward current sheet in the former case and augmenting it in the latter.

Following *Hunt et al.* [2014], we have then characterized the current sheets in the dawn-noon sector by the inferred meridional ionospheric current per radian of azimuth flowing at the feet of the field lines at the boundaries of the sheets, together with the boundary colatitudes relative to the southern pole. We find that the values of the dawn-noon currents generally lie within the scatter of the corresponding midnight data, such that there is no qualitative difference between the auroral currents flowing across the broad dawn sector from midnight to noon. The current sheet boundaries are located at smaller colatitudes in the near-noon data set than at midnight, however, while the predawn boundaries lie typically in the equatorward range of the midnight data, consistent with an "auroral circle" whose center is displaced from the planet's spin/magnetic axis toward the nightside and dawn, as found in auroral imagery by *Nichols et al.* [2008] and *Carbary* [2012]. Here the boundary data are well lined up by a shift of 3° colatitude toward 4 h LT and have applied this transformation to our data.

Averaging the boundary currents for the dawn-noon and midnight data sets in two 180° ranges of southern PPO phase centered at $\Psi_S = 90^\circ$ and 270° , and comparing their (transformed) colatitude profiles, we find that the dawn-noon and midnight profiles are very similar for the range centered on $\Psi_S = 90^\circ$. For the range centered on $\Psi_S = 270^\circ$, however, we find that on average the main upward current is modestly larger by a factor of ~ 1.2 at dawn-noon than at midnight. The adjacent secondary downward current (sheet 3) is also consequently larger at dawn-noon than at midnight by a factor of ~ 2.6 . We have then taken half the sum and half the difference of the $\Psi_S \sim 90^\circ$ and 270° current profiles for both the dawn-noon and midnight data sets to estimate the PPO-independent currents and the PPO-related currents, respectively. Surprisingly, we find that the PPO-independent current profiles are essentially identical within uncertainties, such that we discern no strong LT dependency throughout the dawn sector. These results do not therefore support the view that the broadly distributed subcorotation current is strongly modulated by LT-dependent solar wind currents in the dawn sector. The PPO-related currents are also found to be similar at dawn-noon and midnight, though narrower in colatitude and peaking at slightly higher values at dawn-noon than at midnight. The dawn-noon profile also provides evidence for a PPO-related current of reversed sense but reduced magnitude flowing equatorward of the main PPO-related current, as found in northern data by *Hunt et al.* [2015].

We also investigated the implications of the variations in the averaged properties of main upward current sheet 2 for the power in precipitating auroral electrons and hence auroral emissions, using *Knight's* [1973] theory of auroral electron acceleration. Assuming a fixed magnetospheric source electron population, and considering the difference in power between the two 180° ranges of Ψ_S centered on 90° and 270° , we first find that the power for $\sim 270^\circ$ should exceed that for $\sim 90^\circ$ by factors of ~ 5 and ~ 3 for the dawn-dusk and

midnight data sets, respectively, values that are in good accord with the variations in morning sector auroral power observed by *Nichols et al.* [2010]. Concerning the LT-related differences in power for given Ψ_5 ranges, we have shown that there is essentially no difference in power between the two LT regimes for the 180° range centered on 90°, and only a difference of a factor of ~1.6 larger power at dawn-noon than at midnight for the 180° range centered on 270°, thus giving an overall difference in averaged power of a factor of only ~1.3. This difference is thus inadequate to account for the observed difference in SKR power in the two LT regimes of a factor of ~2.7 from the results of *Lamy et al.* [2009]. Some other feature, such as a systematic variation in the auroral source electron parameters, hotter and/or more tenuous at dawn-noon compared with midnight, must therefore be involved.

Acknowledgments

Work at Leicester was supported by STFC Consolidated Grants ST/K001000/1 and ST/N000749/1, work at UCL-MSSL by STFC Consolidated Grant ST/K000977/1, and work at SINP MSU by RFBF Grant 12-05-00219-a. G.J.H. was supported by STFC Quota Studentship ST/K502121/1. E.J.B. was supported by the award of the Philip Leverhulme Prize. CAPS-ELS operations were supported by ESA via the UK Space Agency. We thank S. Kellock and the Cassini Mag team at Imperial College for access to processed magnetometer data, J.F. Carbary for access to the UV auroral boundary data shown in Figure 3, and L. Lamy for helpful comments on SKR observations. G.J.H. and G.P. acknowledge the support of the International Space Science Institute, as this study was discussed at the international team "Rotational phenomena in Saturn's magnetosphere." Calibrated data from the Cassini mission are available from the NASA Planetary Data System (PDS) at the Jet Propulsion Laboratory (<https://pds.jpl.nasa.gov/>). Specifically, 1 min averaged KRTP magnetic field data as used here can be obtained from PDS volume CO-E/SW/J/S-MAG-4-SUMM-1MINAVG-V1.0, while uncalibrated ELS data as also employed can be obtained from volume CO-E/J/S/SW-CAPS-2-UNCALIBRATED-V1.0.

References

- Andrews, D. J., A. J. Coates, S. W. H. Cowley, M. K. Dougherty, L. Lamy, G. Provan, and P. Zarka (2010), Magnetospheric period oscillations at Saturn: Comparison of equatorial and high-latitude magnetic field periods with north and south SKR periods, *J. Geophys. Res.*, *115*, A12252, doi:10.1029/2010JA015666.
- Andrews, D. J., S. W. H. Cowley, M. K. Dougherty, L. Lamy, G. Provan, and D. J. Southwood (2012), Planetary period oscillations in Saturn's magnetosphere: Evolution of magnetic oscillation properties from southern summer to post-equinox, *J. Geophys. Res.*, *117*, A04224, doi:10.1029/2011JA017444.
- Belenkaya, E. S., S. W. H. Cowley, S. V. Badman, M. S. Blokhina, and V. V. Kalegaev (2008), Dependence of the open-closed field line boundary in Saturn's ionosphere on both the IMF and solar wind dynamic pressure: comparison with the UV auroral oval observed by the HST, *Ann. Geophys.*, *26*, 159–166, doi:10.5194/angeo-26-159-2008.
- Bunce, E. J., S. W. H. Cowley, I. I. Alexeev, C. S. Arridge, M. K. Dougherty, J. D. Nichols, and C. T. Russell (2007), Cassini observations of the variation of Saturn's ring current parameters with system size, *J. Geophys. Res.*, *112*, A10202, doi:10.1029/2007JA012275.
- Bunce, E. J., et al. (2008), Origin of Saturn's aurora: Simultaneous observations by Cassini and the Hubble Space Telescope, *J. Geophys. Res.*, *113*, A09209, doi:10.1029/2008JA013257.
- Bunce, E. J., S. W. H. Cowley, D. L. Talboys, M. K. Dougherty, L. Lamy, W. S. Kurth, P. Schippers, B. Cecconi, P. Zarka, C. S. Arridge, and A. J. Coates (2010), Extraordinary field-aligned current signatures in Saturn's high-latitude magnetosphere: Analysis of Cassini data during Revolution 89, *J. Geophys. Res.*, *115*, A10238, doi:10.1029/2010JA015612.
- Bunce, E. J., et al. (2014), Cassini nightside observations of the oscillatory motion of Saturn's northern auroral oval, *J. Geophys. Res. Space Physics*, *119*, 3528–3543, doi:10.1002/2013JA019527.
- Burton, M. E., M. K. Dougherty, and C. T. Russell (2010), Saturn's internal planetary magnetic field, *Geophys. Res. Lett.*, *37*, L24105, doi:10.1029/2010GL045148.
- Carbary, J. F. (2012), The morphology of Saturn's ultraviolet aurora, *J. Geophys. Res.*, *117*, A06210, doi:10.1029/2012JA017670.
- Cowley, S. W. H. (2000), Magnetosphere-ionosphere interactions: A tutorial review, in *Magnetospheric Current Systems*, *Geophys. Monogr.*, vol. 118, edited by S. Ohtani et al., pp. 91–106, AGU, Washington, D. C.
- Cowley, S. W. H., E. J. Bunce, and R. Prangé (2004a), Saturn's polar ionospheric flows and their relation to the main auroral oval, *Ann. Geophys.*, *22*, 1379–1394, doi:10.5194/angeo-22-1379-2004.
- Cowley, S. W. H., E. J. Bunce, and J. M. O'Rourke (2004b), A simple quantitative model of plasma flows and currents in Saturn's polar ionosphere, *J. Geophys. Res.*, *109*, A05212, doi:10.1029/2003JA010375.
- Cowley, S. W. H., C. S. Arridge, E. J. Bunce, J. T. Clarke, A. J. Coates, M. K. Dougherty, J.-C. Gérard, D. Grodent, J. D. Nichols, and D. L. Talboys (2008), Auroral current systems in Saturn's magnetosphere: Comparison of theoretical models with Cassini and HST observations, *Ann. Geophys.*, *26*, 2613–2630, doi:10.5194/angeo-26-2613-2008.
- Gurnett, D. A., et al. (2010), A plasmopause-like density boundary at high latitudes in Saturn's magnetosphere, *Geophys. Res. Lett.*, *37*, L16806, doi:10.1029/2010GL044466.
- Hunt, G. J., S. W. H. Cowley, G. Provan, E. J. Bunce, I. I. Alexeev, E. S. Belenkaya, V. V. Kalegaev, M. K. Dougherty, and A. J. Coates (2014), Field-aligned currents in Saturn's southern nightside magnetosphere: Subrotation and planetary period oscillation components, *J. Geophys. Res. Space Physics*, *119*, 9847–9899, doi:10.1002/2014JA020506.
- Hunt, G. J., S. W. H. Cowley, G. Provan, E. J. Bunce, I. I. Alexeev, E. S. Belenkaya, V. V. Kalegaev, M. K. Dougherty, and A. J. Coates (2015), Field-aligned currents in Saturn's northern nightside magnetosphere: Evidence for interhemispheric current flow associated with planetary period oscillations, *J. Geophys. Res. Space Physics*, *120*, 7552–7584, doi:10.1002/2015JA021454.
- Jackman, C. M., and S. W. H. Cowley (2006), A model of the plasma flow and current in Saturn's polar ionosphere under conditions of strong Dungey cycle driving, *Ann. Geophys.*, *24*, 1029–1055, doi:10.5194/angeo-24-1029-2006.
- Jia, X., and M. G. Kivelson (2012), Driving Saturn's magnetospheric periodicities from the upper atmosphere/ionosphere: Magnetotail response to dual sources, *J. Geophys. Res.*, *117*, A11219, doi:10.1029/2012JA018183.
- Jia, X., M. G. Kivelson, and T. I. Gombosi (2012), Driving Saturn's magnetospheric periodicities from the upper atmosphere/ionosphere, *J. Geophys. Res.*, *117*, A04215, doi:10.1029/2011JA017367.
- Jinks, S. L., et al. (2014), Cassini multi-instrument assessment of Saturn's polar cap boundary, *J. Geophys. Res. Space Physics*, *119*, 8161–8177, doi:10.1002/2014JA020367.
- Kellett, S., C. S. Arridge, E. J. Bunce, A. J. Coates, S. W. H. Cowley, M. K. Dougherty, A. M. Persoon, N. Sergis, and R. J. Wilson (2011), Saturn's ring current: Local time dependence and temporal variability, *J. Geophys. Res.*, *116*, A05220, doi:10.1029/2010JA016216.
- Knight, S. (1973), Parallel electric fields, *Planet. Space Sci.*, *21*, 741–750, doi:10.1016/0032-0633(73)90093-7.
- Lamy, L., B. Cecconi, R. Prangé, P. Zarka, J. D. Nichols, and J. T. Clarke (2009), An auroral oval at the footprint of Saturn's kilometric radio sources, collocated with the UV aurorae, *J. Geophys. Res.*, *114*, A10212, doi:10.1029/2009JA014401.
- Lamy, L., et al. (2010), Properties of Saturn kilometric radiation measured within its source region, *Geophys. Res. Lett.*, *37*, L12104, doi:10.1029/2010GL043415.
- Lamy, L., B. Cecconi, P. Zarka, P. Canu, P. Schippers, W. S. Kurth, R. L. Mutel, D. A. Gurnett, D. Menietti, and P. Louarn (2011), Emission and propagation of Saturn kilometric radiation: Magnetoionic modes, beaming pattern, and polarization state, *J. Geophys. Res.*, *116*, A04212, doi:10.1029/2010JA016195.

- Lundin, R., and I. Sandahl (1978), Some characteristics of the parallel electric field acceleration of electrons over discrete auroral arcs as observed from two rocket flights, *ESA Eur. Sound. Rocket, SP-135*, 125–136.
- Mutel, R. L., J. D. Menietti, D. A. Gurnett, W. Kurth, P. Schippers, C. Lynch, L. Lamy, C. Arridge, and B. Cecconi (2010), CMI growth rates for Saturnian kilometric radiation, *Geophys. Res. Lett.*, *37*, L19105, doi:10.1029/2010GL044940.
- Nichols, J. D., J. T. Clarke, S. W. H. Cowley, J. Duval, A. J. Farmer, J.-C. Gérard, D. Grodent, and S. Wannawichian (2008), Oscillation of Saturn's southern auroral oval, *J. Geophys. Res.*, *113*, A11205, doi:10.1029/2008JA013444.
- Nichols, J. D., B. Cecconi, J. T. Clarke, S. W. H. Cowley, J.-C. Gérard, A. Grocott, D. Grodent, L. Lamy, and P. Zarka (2010), Variation of Saturn's UV aurora with SKR phase, *Geophys. Res. Lett.*, *37*, L15102, doi:10.1029/2010GL044057.
- Southwood, D. J., and M. G. Kivelson (2007), Saturn magnetospheric dynamics: Elucidation of a camshaft model, *J. Geophys. Res.*, *112*, A12222, doi:10.1029/2007JA012254.
- Southwood, D. J., and M. G. Kivelson (2009), The source of Saturn's periodic radio emission, *J. Geophys. Res.*, *114*, A09201, doi:10.1029/2008JA013800.
- Southwood, D. J., and S. W. H. Cowley (2014), The origin of Saturn magnetic periodicities: northern and southern current systems, *J. Geophys. Res. Space Physics*, *119*, 1563–1571, doi:10.1002/2013JA019632.
- Talboys, D. L., C. S. Arridge, E. J. Bunce, A. J. Coates, S. W. H. Cowley, and M. K. Dougherty (2009a), Characterization of auroral current systems in Saturn's magnetosphere: High-latitude Cassini observations, *J. Geophys. Res.*, *114*, A06220, doi:10.1029/2008JA013846.
- Talboys, D. L., C. S. Arridge, E. J. Bunce, A. J. Coates, S. W. H. Cowley, M. K. Dougherty, and K. K. Khurana (2009b), Signatures of field-aligned currents in Saturn's nightside magnetosphere, *Geophys. Res. Lett.*, *36*, L19107, doi:10.1029/2009GL039867.
- Talboys, D. L., E. J. Bunce, S. W. H. Cowley, C. S. Arridge, A. J. Coates, and M. K. Dougherty (2011), Statistical characteristics of field-aligned currents in Saturn's nightside magnetosphere, *J. Geophys. Res.*, *116*, A04213, doi:10.1029/2009JA016102.